

NUCOBAM

Innovation Action (IA)

This project has received funding from the European Union's Horizon 2020 research and innovation programme under grant agreement No 945313

Start date: 2020-10-01 Duration: 48 Months



Scientific article

Authors: [... Kamel ETTAIEB (Framatome - do not use), Milan Konstantinovic (SCK-CEN), Didier BARDEL (Framatome), Guillaume BADINIER (Framatome)

NUCOBAM - Contract Number: 945313

Project officer: Cristina FERNANDEZ RAMOS

Document title	Scientific article
Author(s)	Kamel ETTAIEB, Milan Konstantinovic (SCK-CEN), Didier BARDEL (Framatome), Guillaume BADINIER (Framatome)
Number of pages	0
Document type	Deliverable
Work Package	WP4
Document number	D4.4
Issued by	Framatome - do not use
Date of completion	2024-09-30 23:28:59
Dissemination level	Public

Summary

Comparison of irradiation results with results on conventional materials available in the literature

Approva

Date	Ву
2024-09-30 23:31:49	Kamel ETTAIEB (Framatome - do not use)
2024-09-30 23:36:08	Dr. Myriam BOURGEOIS (CEA)

M.J. Konstantinović^{a,*}, D. Bardel^b, W. Van Renterghem^a, S. Van Dyck^a, G. Badinier^b, K. Ettaieb^c, A. Revuelta^d, T.Riipinen^d

^aStudiecentrum voor Kernenergie/Centre d'Etude de l'Energie Nucléaire (SCK CEN), Boeretang 200, B-2400 Mol, Belgium

^bFramatome, 2 rue Professeur Jean Bernard, 69007 Lyon, France
^cFramatome, Centre Technique, Rue Louis Alphonse Poitevin, 71380 CHALON SUR
SAONE, France

 dVTT Technical research center of Finland Ltd, Kivimiehentie 3, Espoo, Finland

Abstract

This study was conducted on 316L material produced by additive manufacturing, laser powder bed fusion process, with four heat treatment conditions: stress relief, low and high temperature solution annealing and hot isostatic pressing. The materials were neutron irradiated in the Belgian material testing reactor BR2 at 300 °C and with a dose up to about 4 dpa. Charpy impact and tensile test results revealed that all materials gradually harden and loose ductility with increasing dose. At the highest dose, the decrease of absorbed energy is the largest for the high temperature solution annealed sample, of about 60 % from its initial value, while the stress relieved material exhibits the smallest reduction, of about 20 % from its initial value. Yield stress is observed to be more sensitive to neutron dose than tensile stress. The bigger initial hardening, the smaller irradiation hardening. In addition, all 316L additive manufactured materials reach the same hardening level of about 600 MPa at a dose of about 4 dpa. Most probably, initial contribution to hardening, originating from dislocation density differences between material batches, is gradually overtaken by irradiation induced defect contribution that becomes the most dominant contribution to hardening at 4 dpa and explains the convergence of yield stress values. Depending of the dose and the heat treatment conditions, the yield stress values of all batches lay below the material constitutive model of irradiated solution annealed 316L stainless steel. These results could potentially indicate a beneficial effect of the additive manufacturing process to irradiation hardening resistance of 316L stainless steel.

Email address: mkonstan@sckcen.be (M.J. Konstantinović)

^{*}Corresponding author

1. Introduction

Rapid advancements in additive manufacturing (AM) technologies are driven by the opportunity for industries to revolutionize the global part manufacturing and supply chain landscape. They are now opening up opportunities for nuclear industry to build complex components while reducing cost, time, energy consumption and carbon footprint [1, 2]. In that context, austenitic stainless steels are one of the main target to be used for the reactor core and primary coolant system components, since they offer a good combination of strength, ductility, and toughness, together with low sensitivity to oxidation-corrosion and superior irradiation resistance [3, 4]. Moreover, these steels produced by Laser Powder Bed Fusion (L-PBF) process are considered to be suitable candidates for the production of nuclear power plant (NPP) reactor core components [5, 6, 7, 8]. One of the reasons for this interest is that L-PBF process prevents the formation of excessive ferrite phase during rapid cooling, and that 316L stainless steels produced by this process maintain their high oxidation resistance, at an equivalent level or even better than their wrought counterpart [9]. The microstructure of 316L produced by LPBF process is different from that of conventionally manufactured 316L steel, as a result of a specific layer-by-layer construction, the use of a powder feedstock, local melting and rapid solidification processes [1]. Specific microstructural features of AM 316L usually include columnar grains elongated along the building direction, intragranular solidification cells, dislocation substructures at cell boundaries, oxide nanoparticles and increased porosity compared to wrought alloys [6, 7, 10]. The impact of these microstructural features to tensile and fracture properties has been evaluated in much detail in out-of-pile conditions [11, 12, 9, 13, 14, 8, 15, 16, 17]. Most of the mechanical test results are observed to depend on the grain orientation and porosity anisotropy, with some sensitivity to oxide nanoparticles coarsening and grain boundary segregation. As compared to conventionally produced 316L, the 316L L-PBF offers, in as-built state, a very high strength (600 MPa) together with high elongation values (> 20%) [18]. This tradeoff is dependent on the size and orientation of the dislocation cell structures, but is mostly affected by the post-build thermal treatment that could reduce or suppress these cells [18]. From Charpy impact tests, absorbed energy of 316L L-PBF is usually found to be below the values typically observed for wrought 316L stainless steel [16, 17] with a scatter that can be quite high (20 to 200 J) depending on the manufacturing process parameters [22]. For this alloy it was also demonstrated that both fracture toughness at crack initiation and crack propagation rates can be positively correlated to Charpy absorbed energies at crack initiation and crack propagation (as assessed through instrumented Charpy testing), respectively, indicating that the same physical mechanism is responsible for cracking in two type of tests [17].

Despite this significant progress, it is important to consider that in most cases the replacement of standard NPP reactor core component manufactured by the L-PBF technology should include a demonstration of the quality and safety of the materials under representative NPP operating conditions (i.e. with corrosive and irradiation environments) [23]. Literature already exists in an irradiation context for 316L L-PBF, but it is usually focusing on swelling and microstructural evolutions due to the type of particles used (ions or protons) [24, 25, 26, 27]. These works highlight that the mechanisms in 316L L-PBF are similar to the one in the wrought counterpart, but with some quantitative variations due to the initial microstructure features. For example, during swelling analysis, at temperatures above 300 °C, a comparable low rate between wrought and L-PBF heat treated samples is observed, while suggesting a tendency towards a reduction of the resistance to swelling when the microstructure contained initial dislocation densities [27]. On the other hand, these microstructural investigations after ion irradiation up to 5 dpa indicate that dislocation cellular wall structures may act as effective sinks for irradiation induced defects and may reduce the final dislocation loop density induced by irradiation. Essentially, no significant drawback regarding the use of 316L L-PBF materials in nuclear environment were identified with these ions irradiation programs. Despite the strong interest, these studies suffer from two disadvantages: (i) a high amount of characterization are needed at the local scale to try to predict a global (volume) property of the alloys, (ii) similarly, any bulk mechanical tests, such tensile test, is inhibited by the local nature of these radiation tests.

To go beyond investigations based on ion irradiation and to provide quantitative assessment of bulk properties, neutron irradiation are required. Such kind of irradiation and post irradiation examinations (PIE) are scarce and only limited information is provided [28, 29, 4]. Byun et.al. [4], conducted neutron irradiation at 300 °C and 600 °C with dose levels of 0.2 and 2 dpa. Concerning irradiation at 300 °C temperature, the radiation hardening was observed to be lower in as-build and stress-relieved L-PBF stainless steels than in the weaker solution-annealed L-PBF and the reference wrought steel [4]. Despite significant ductility drop in the sample with as-built condition, no embrittlement (i.e. failure before yielding) was observed within the irradiations conditions explored by the authors, suggesting good applicability of 316L L-PBF for in-core reactor applications [4]. The present work, executed within the NUCOBAM EU program [30] is, in a way, a continuation of Byun's et.al. investigation [4], as it is providing new bulk mechanical results to evaluate the ability of 316L L-PBF to withstand neutron irradiation. In this study, in addition to stress relieve and low-temperature annealed samples, the high temperature annealed and HIP-ed samples are also investigated, complementing the previous works.

Post-built stress relieve, solution annealing and high temperature HIP treatments of the L-PBF samples are selected for neutron irradiation and post irradiation examination in order to provide additional information on the irradiation sensitivity to the initial L-PBF microstrures. As described in the next sessions, by reaching several fluence levels in the range of 0.5 to 4 dpa, this work brings additional insight on the damage kinetics in 316L L-PBF stainless steel.

element (wt.%)	С	Si	Р	S	Cr	Mn	Ni	Co	Mo	О	N	Fe
316L ss reference	0.044	0.53	0.022	0.009	17.0	1.79	12.8	0.07	2.68			bal
316L ss powder	0.02	1	0.01	0.004	17.8	0.8	12.6	0.03	2.30	0.09	0.02	bal

Table 1: Nominal composition of the 316 stainless steel reference and the 316L powder used in this study.

Batch	Process	Post-built treatment	Metallurgical state	Porosity	Direction
AM316-SR	L-PBF	650 (° C)	As-build AM	< 1%	Z ⊥building platform
AM316-SA1066	L-PBF	1066 (°C)	Annealed, partially recrystallized	< 1%	$Z \perp$ building platform
AM316-SA1150	L-PBF	1150 (°C)	Fully recrystallized	< 1%	$Z \perp$ building platform
AM316-HIP	L-PBF	$1150(^{0}C), P > 100 MPa$	Fully recrystallized	< 1%	$Z \perp$ building platform
Reference	Cold worked bar		Cold-worked	No	longitudinal

Table 2: Materials and metallurgical conditions.

2. Experimental

2.1. Materials

Four identical platforms containing different test specimens were printed using SLM Solutions 125HL LPBF machine using standard 316L scanning strategy and process parameters defined by the machine manufacturer for 30 μm layer thickness. Argon was used as a shielding gas for the duration of the manufacturing process. Chemical composition of the used powder is given in Table 1. The machine was operated under nominal parameters to get (i) a porosity level lower than 1% [31], (ii) and an as-built microstructure typical of 316L described in the literature [9, 18]. Each set of manufactured samples was subjected to a different heat treatment cycle: 1) stress relief at 650 0 C (batch AM316-SR), 2) solution anneal at 1066 0 C (batch AM316-SA1066), 3) solution anneal at 1150 0 C (batch AM316-SA1150) and 4) hot isostatic pressing treatment with pressure > 100 MPa (batch AM316-HIP). An additional batch, from a conventional cold-worked 316L material bar, was also selected for comparison purposes, see Table 1.

From these batches, three kinds of samples were extracted by conventional machining: (1) Sub-sized (3x4x27 mm) Charpy samples, for tests at room temperature according to ISO 14556 standard [32], (2) flat mini tensile test samples (1.5x4.2x18 mm^3) for tensile tests at 300 0 C according to ASTM E21 standard [33], and (3) transmission electron microscopy samples in the form of thin plates (0.5 mm thickness).

2.2. BR2 irradiation

The goal of NUCOBAM irradiation program is to study bulk properties of L-PBF 316L materials in representative reactor conditions. For that purpose neutron irradiation was performed in the BR2 materials testing reactor of SCK-CEN at 300 0 C. The samples were placed in the standard aluminium capsule, with a total length of 80 mm. Each capsule accommodated two identical sample sets (two batches and the reference samples) in two floor layout, see Fig. 1. Each capsule floor contains: Two mini-Charpy AM specimens, four tensile specimens and two TEM plates of AM material. In addition, besides standard

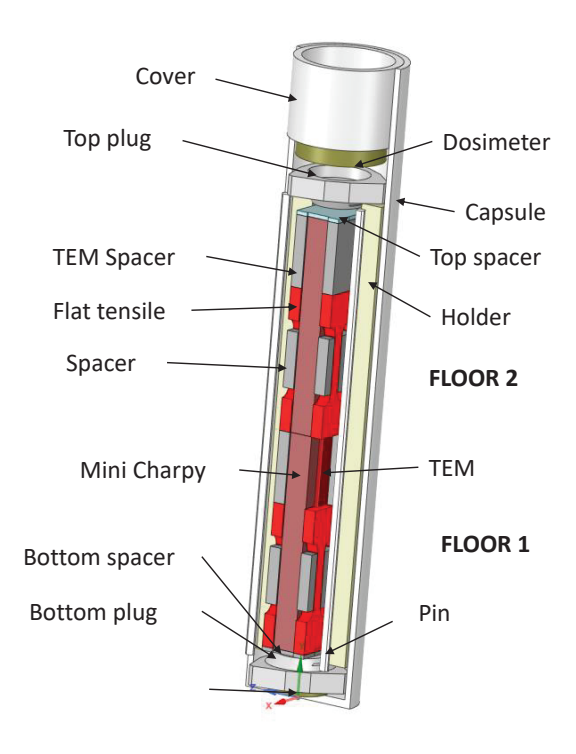


Figure 1: Drawing of the BAMI capsule.

capsule inner parts, fillers and spacers are introduced in the capsule to reduce the open space and to improve thermal conductivity. The capsules with samples were loaded in an un-instrumented basket for material irradiation (BAMI) that is positioned inside six-plate fuel element.

This irradiation condition provides neutron flux up to $2.5 \times 10^{14} n/cm^2 s$ (E > 1 MeV), and enables to reach neutron dose of about 0.7 dpa within one BR2 cycle (typically 4 week long). The capsules were gas filled and sealed, in which case the irradiation temperature is determined by neutron heat contribution at specific irradiation position, the mass of the samples, the composition of the gas as well as the spacing between the samples and the cold wall of the capsule. Maximum two capsules per channel were irradiated at flat neutron flux position (around mid-plane), allowing stable and uniform irradiation temperature. Total neutron fluence is obtained from the Fe dosimeter prepared from certified reference material IRMM-524A. Each capsule contained two dosimeters in the form of circular disk, positioned at the top and at the bottom of the capsule.

The summary of the NUCOBAM irradiation conditions is presented in Table 3.

Capsule	Materials	No. of cycles	Irr. T (⁰ C)	Dose (dpa)
NU01	AM 316-SR, AM 316-SA 1066, CW 316-Ref.A	1	317 ± 40	0.84
NU02	AM 316-SA 1150, AM 316-HIP, CW 316-Ref.B	1	280 ± 25	0.56
NU03	AM 316-SR, AM 316-SA 1066, CW 316-Ref.A	3	303 ± 21	2.2
NU04	AM 316-SA 1150, AM 316-HIP, CW 316-Ref.B	3	307 ± 14	2.3
NU05	AM 316-SR, AM 316-SA 1066, CW 316-Ref.A	6	300 ± 29	4.2
NU06	AM3 16-SA 1150, AM 316-HIP, CW 316-Ref.B	6	291 ± 35	3.8
NU07	AM 316-SR, AM 316-SA 1066, CW 316-Ref.A	4	309 ± 42	3.0
NU08	AM316-SA 1150, AM 316-HIP, CW 316-Ref.B	4	297 ± 36	2.9

Table 3: NUCOBAM irradiation conditions

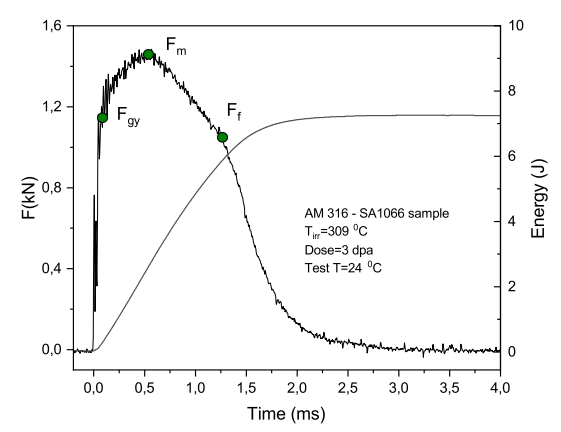


Figure 2: Typical result of an instrumented Charpy impact test, showing load vs time and absorbed energy of NUCOBAM AM 316 solution annealed at $1066~^{0}\mathrm{C}$ specimen irradiated to 3 dpa.

2.3. Mechanical tests

Charpy impact tests were performed with a Wolpert PW5 test setup, equipped with ISO instrumented 10 kN tup, with available energy of 25 J, and the speed of 3.83 m/s to produces results according to ISO 14556 standard [32]. This instrument utilizes sub-sized Charpy sample with a notch of 1 mm through the specimen width, which is broken in three-point bending mode. The fracture energy is determined from instrumented impact measurements of the load-time record, recorded at room temperature.

Typical extracted parameters are presented in Fig. 2. They are: (i) The onset of the general yield load (F_{gy}) , (ii) the maximum load (F_m) , associated to the macroscopic crack initiation, and (iii) the force needed for instable crack propagation (F_f) . From this information the energy can be partitioned between preand post-maximum load energies (including shear lip formation energy) that represents initiation and propagation energies. For each experimental condition, two Charpy specimens were tested. An error bar of extracted absorbed energy is estimated to be of about 0.25 J.

After the test, an image of the broken specimen is taken, and the lateral expansion is measured by caliper. The amount by which the specimen deforms

after the Charpy impact test is measured and expressed as millimeters of lateral expansion. The bigger the lateral expansion, the higher the ductility of the specimen.

Tensile tests were performed in an Instron 1341 machine, with a constant crosshead speed of $0.1~\rm mm\cdot min^{-1}$, which corresponds to a strain rate of $1.4~\rm x~10^{-4}~\rm s^{-1}$. The flat tensile specimens were 18 mm long, with a rectangular gauge section of $1.5~\rm mm~x~1.6~mm$, and $7.2~\rm mm$ in length. The tensile test results of AM L-PBF samples and the reference samples were obtained by averaging two and four measurement results, respectively. Typically, the error bar of the tensile test in the machine used is about 6~%. However, since the tests were performed on small flat specimens, the error bar of was estimated to be the largest difference between the results of different tests which were performed on the same material and under the same conditions (if larger than 6~%).

2.4. Scanning electron and transmission electron microscopy

Scanning electron microscopy (SEM) examination of the fracture surfaces is performed with a JEOL 7100 field emission gun instrument working in both secondary electron and backscattering electron imaging mode. This instrument is placed in the hot cell and it is equipped with a Bruker energy dispersive X-ray detection system (EDX). Transmission electron microscopy (TEM) was performed on 300 keV JEOL JEM-ARM300F2 instrument, equipped with scanning detection mode. TEM images were taken in both TEM and STEM imaging modes and chemical mapping is obtained using energy dispersive spectrometry (EDS) JEOL DUAL DRY SD 320. TEM samples are produced by standard electro-polishing technique and are used to check the consistency of initial sample microstructure with the literature [18].

3. Results and discussion

3.1. TEM of unirradiated alloys

Microstructure features of 316L L-PBF samples and that of the reference sample taken under the low and high magnification conditions are shown in Fig. 3. AM 316-SR material contains numerous sub-grain features composed mainly of cellular structures formed by dislocations and precipitates. These substructures are clearly distinguishable from the characteristic microstructure of the reference material (cast cold-work 316L stainless steel), which consists of a high dislocation density and twins. The cellular dislocation structure is in a very good agreement with previous reports [18, 19]. The cellular structures gradually disappear in AM 316-SA 1066 and dislocation annealing increases in the AM316 SA 1150 material, which is qualitatively consistent with the work of Salman et.al. [20]. The AM 316 HIP material only contains dislocations at sites where the dislocation movement is blocked, like grain boundaries and precipitates. The high density of tangled dislocations inside the cell walls of AM316-SR sample is found to provide a strong contribution to hardening, explaining at least in part the high yield strength of this material, see section 3.3. Thermal annealing at

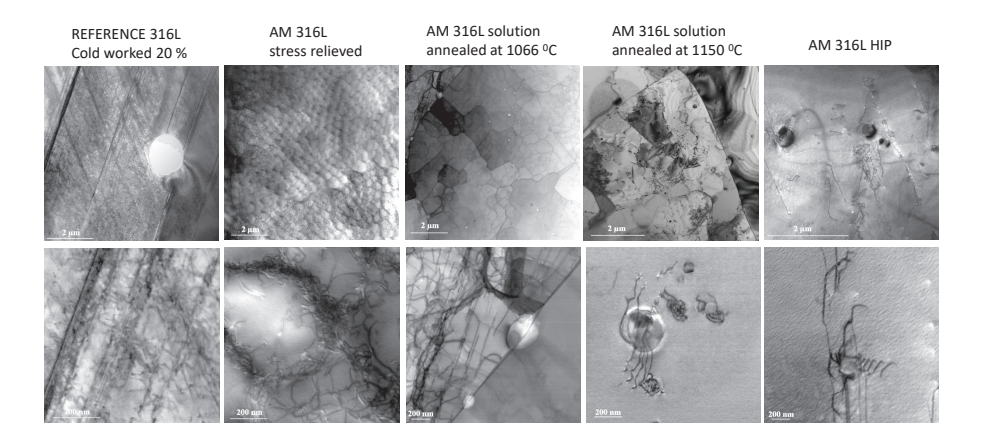


Figure 3: STEM images of unirradiated additive manufacture materials and that of the reference sample taken with low (top row) and high magnification (bottom row).

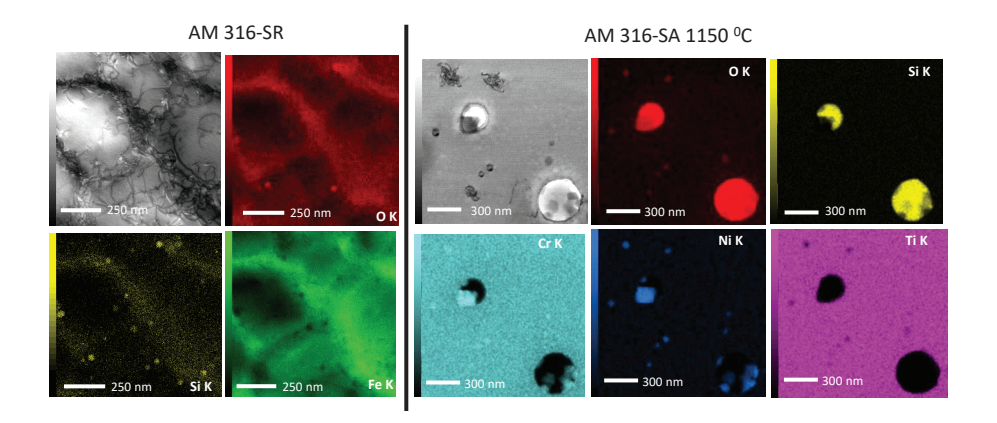


Figure 4: Chemical mapping by TEM-EDX of AM 316-SR and AM 316-SA 1150 samples.

high temperature in the AM 316-SA 1066 and AM 316-SA 1150 samples causes a gradual disappearance of dislocations, leading to a drop in yield strength and increase of the ductility.

Besides dislocations, an analysis of the precipitates has been performed in AM 316-SR and AM 316-SA 1150 samples. In AM 316-SR, numerous small Si-O precipitates are observed, see Fig. 4. They have an average diameter of about 20 nm and the number density of the order of $5 \times 10^{20} m^{-3}$ (these values need to be taken as being very approximate because there is insufficient statistics and the sample thickness was only estimated to be 100nm based on the absorption contrast). Chemical mapping indicates that these small precipitates are mainly located at the dislocation cell boundaries. In AM 316-SA 1150, Si-O precipitates grew, most probably as a consequence of thermal treatment. They reach an average size of the order of 300 nm and their number density decreases to about $1 \times 10^{19} m^{-3}$. Besides Si-O precipitates, small precipitates composed of Cr, Mn, Ti, Al, O elements are also observed. These results are also in an excellent agreement with previous findings [21].

3.2. Charpy impact test results

The evolution of absorbed energy with the irradiation dose of 316L LPB samples are shown in Fig. 5a). The data are normalized to unirradiated values. For each experimental condition two Charpy specimens were tested. For both unirradiated and neutron irradiated specimens, load vs time of the same specimen condition almost overlap, demonstrating excellent reproducibility. Absorbed energy gradually decreases with increasing dose, indicating gradual loss of ductility in all samples. At the highest dose of about 4 dpa, the relative decrease of absorbed energy is the largest for AM316-SA1150 material. Absorbed energy reduces to about 60 % from its initial value. AM316-SR material exhibits the smallest reduction, of about 20 % from its initial value. AM316-SA1066 and AM316-HIP materials exhibit an intermediate behavior, with AM316-SA1066 and AM316-SA1150 energies being similar to AM316-SR and AM316-SA1150, respectively.

Lateral expansion of all tested Charpy samples versus neutron dose is presented in Fig. 5b). Lateral expansion values decrease by increasing neutron dose in all batches, which indicates the loss of ductility due to accumulation of the material damage. Overall trend is similar to the absorbed impact energy measured from the Charpy impact test.

SEM images of the fracture surface fragments taken from the highest dose Charpy samples are presented in Fig. 6. The reduction of lateral expansion is accompanied with the increase of fracture surface flatness. In all samples, dimple structures are clearly observed, indicating ductile fracture. From the images taken under low magnification conditions, it appears that grain boundary failure start to contribute in the samples having low absorbed energy, namely AM316-SA1150 and AM316-HIP samples. However, ductile - grain boundary fracture appearance is also observed in unirradiated alloys and was previously reported in the literature as being the consequence of preferential localization of oxide particles at grain boundaries after recrystallization annealing [16]. Finally,

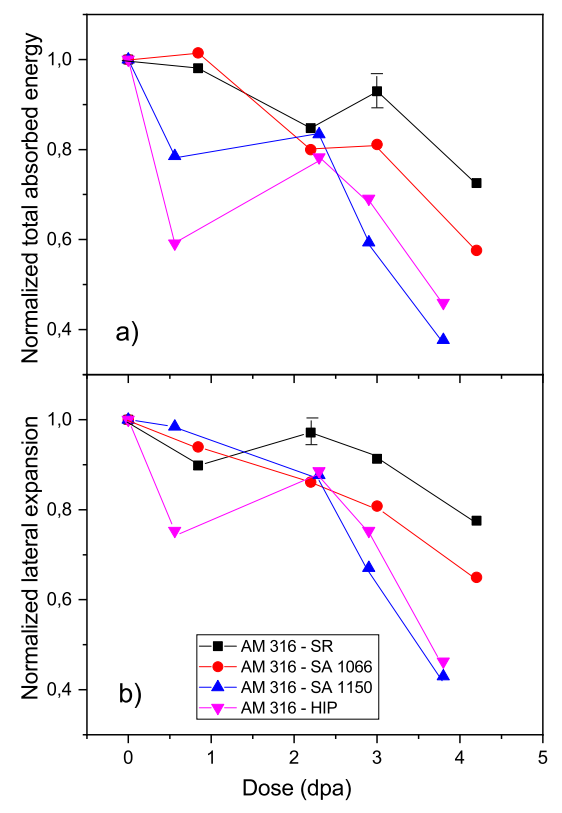


Figure 5: (a) Normalized absorbed energy and b) normalized lateral expansion after Charpy impact test vs dose of 316L L-PBF samples.

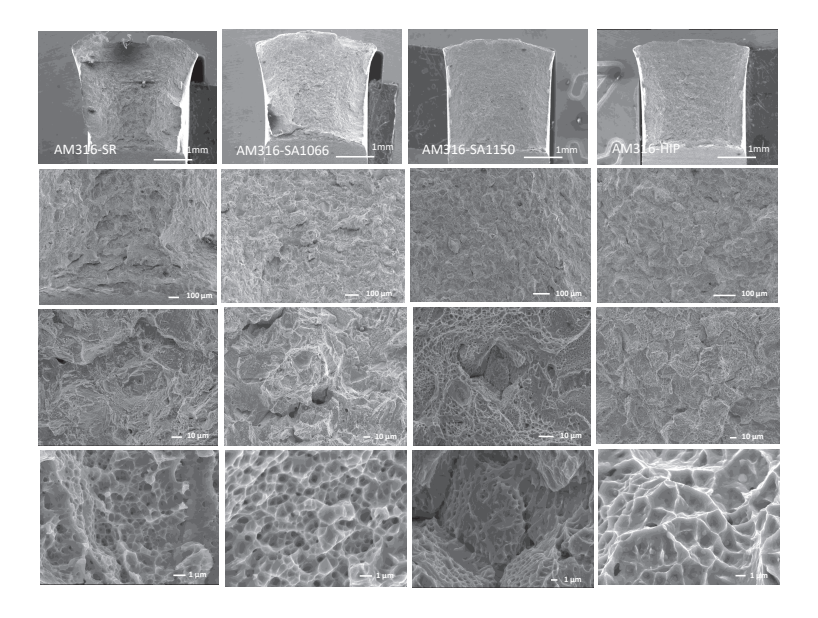


Figure 6: SEM images of the fracture surface of high dose irradiated M316L L-PBF samples after Charpy impact test.

the average size of dimple craters is observed to be the largest in AM316-HIP, most probably due to its large precipitates acting as preferential sites for crack initiation and microvoid nucleation.

3.3. Tensile test results

Concerning tensile tests, load versus displacement curves, which were obtained at 300 °C from both unirradiated and neutron irradiated specimens, are presented in Fig. 7. The results from 316L L-PBF specimens from four different batches, as well as that of the reference material are shown in Fig. 7. Stress versus strain curves are used to extract the standard tensile parameters such as yield stress, ultimate tensile stress, fracture stress, uniform elongation and total elongation. Yield stress and ultimate tensile stress values of all investigated alloys are presented in Fig. 8a) and b), respectively. Neutron irradiation causes hardening in all investigated alloys including the reference. Yield stress is observed to be more sensitive to neutron dose in comparison to tensile stress, Fig. 8. The bigger initial hardening, the smaller irradiation hardening. Interestingly, all 316L L-PBF alloys reach the same yield strength of about 600 MPa at the highest irradiation dose of about 4 dpa. This result suggests that neutron induced defects provide the most dominant contribution to hardening at 4 dpa. Most probably, initial contribution to hardening, originating from dislocation density differences between 316L L-PBF alloys is gradually overtaken by irradiation induced defect. The evolution of yield stress with dose for all investigated alloys are is presented in Fig. 9 to highlight this convergence.

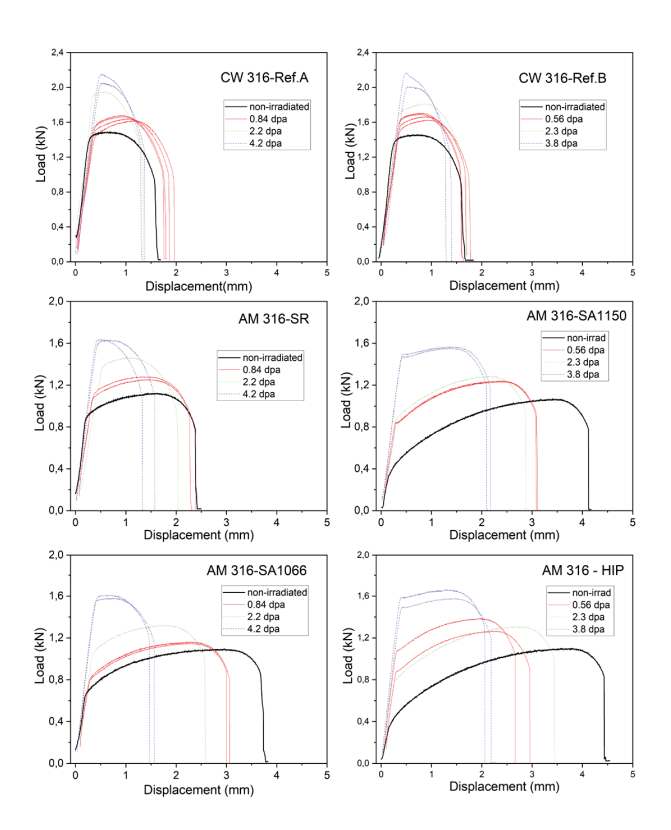
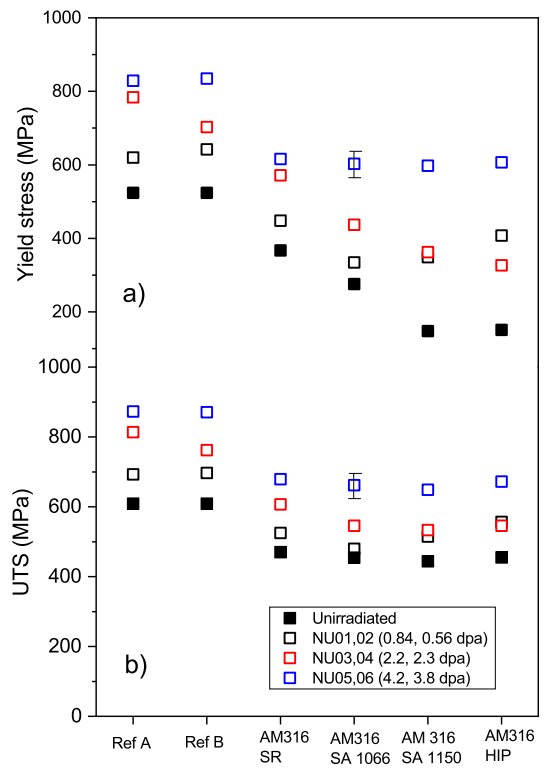


Figure 7: Load versus displacement from tensile tests of 316L L-PBF and CW 316L reference samples



Ref A Ref B AM316 AM316 AM316 AM316 SR SA 1066 SA 1150 HIP
Figure 8: a) Yield stress and b) ultimate tensile stress of unirradiated and neutron irradiated 316L L-PBF and CW 316L reference samples.

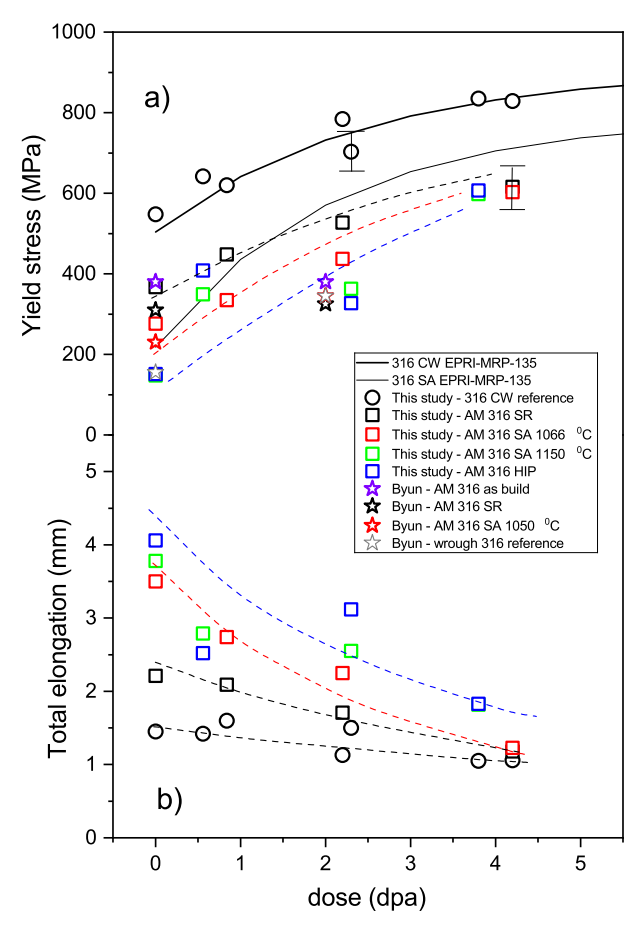


Figure 9: a) Yield stress and b) total elongation versus dose for all investigated 316L L-PBF and CW 316L samples, compared to the literature data. Dashed lines are guide for an eye.

To start analyzing the tensile 316L L-PBF data obtained in this study, the yield stress (YS) of the reference sample is plotted and compared to the material constitutive model of irradiated 316 cold work stainless steel, following EPRI material reliability program MRP-135 [34]. An exponential equation with the form $YS = A0 + A1(1 - e^{-A2*d})$ is used, where d is a dose in dpa and coefficients are defined in Tables 3-6 and 3-7 of Ref.[34] for cold-worked 316L and solution annealed 316L, respectively. All experimental points from our reference material agree with the EPRI model within the error bar. This proves that irradiation was successfully conduced at irradiation temperature close to the 300 °C target. By increasing the dose, all 316L L-PBF materials gradually harden and the initial difference in strength vanishes at about 4 dpa. Hardening values at about 1 and 2 dpa are found to be in a very good agreement with previous measurements from Byun et.al. for comparable heat treatment conditions [4]. Above about 1 dpa, yield stress values of all 316L L-PBF batches lay below the constitutive model for irradiated 316 solution annealed stainless steel. These results possibly indicate the existence of beneficial effect of additive manufacturing to 316L material resistance to irradiation induced hardening. This conclusion is consistent with the arguments provided by Shang et.al. [18]. They observed a significant reduction of dislocation loop density in 316L L-PBF sample as compared to conventional coarse grain microstructure and argue that the cellular walls (with high dislocations density) tend to absorb irradiation-induced dislocation loops serving as effective defect sinks.

Similarly to the yield stress, elongation at fracture is also converging to a comparable deformation levels at 4 dpa, suggesting that the initial microstructure has a limited effect on the ductility drop at that level of irradiation. Surprisingly, the ductility effects are somewhat different from impact toughness test results, as the decrease in absorbed energy is significantly larger for samples which were post-treated at high temperature (AM316-1150 and AM316-HIP, see Fig. 5). Such behavior could be the consequence of a coarser precipitate size, induced by high temperature annealing treatments, see Fig. 4. Indeed, the large precipitates may act as advert crack initiation points that may be not activated during static tensile tests.

4. Conclusions

An irradiation campaign was performed in the framework of the EU project NUCOBAM on 316L stainless steel produced by laser powder bed fusion. These experiments were designed in order (i) to investigate the mechanical bulk properties of the austenitic 316L stainless steel after neutron irradiation, (ii) to study the defect evolution with post-manufacturing heat treatment, (iii) and to discuss the concomitant loss of ductility and hardening with neutron irradiation. Neutron irradiation experiments where performed in the material testing reactor BR2 of SCK CEN, utilizing the BAMI capsules that integrated several sample batches, including a cold-work reference. Pre- and post-irradiation experiments were performed, including Charpy impact and tensile tests as well as

the microstructural investigations based on scanning electron microscopy and transmission electron microscopy. The main findings are:

- No sample suffered from any embrittlement effects i.e. fracture in the elastic domain. Concerning ductility the first observation is that, consistently to tensile strength, the elongation tends to converge to a point similar to the cold-worked wrought alloy. In all Charpy 316L L-PBF samples, the increase of neutron dose caused gradual decrease of absorbed energy: at the highest dose of about 4 dpa, the relative decrease of absorbed energy is the largest for recrystallized material batch.
- Despite variation between initial conditions in terms of microstructure and yield stress, neutron irradiation causes hardening in all investigated alloys, with a converging yield stress for all alloys of about 600 MPa after 4 dpa. By increasing the dose, all 316L L-PBF materials gradually harden. Above about 1 dpa, yield stress values of all 316L L-PBF batches lay below MRP-135 constitutive model for irradiated 316 solution annealed stainless steel. These results could potentially indicate a beneficial effect of the additive manufacturing process to irradiation hardening resistance of 316L stainless steel, consistently with literature hypothesis on sinks effects produced by L-PBF microstructure.
- This study does not highlight the positive impact of HIP treatment regarding in-pile mechanical properties, since no significant difference is observed between AM316-SA1150 and AM316-HIP samples (no impact of the porosity difference).

Acknowledgements This project has received funding from the European research and training programme 2014-2018 under grant agreement No. 945313 (NUCOBAM project).

References

- [1] W.E. Frazier Metal additive manufacturing: a review J. Matls. Eng. Perform., 23 (2014) 1917-1928.
- [2] W.J. Sames, F.A. List, S. Pannala, R.R. DeHoff, S.S. Babu, The metallurgy and processing science of metal additive manufacturing Int. Matls. Rev., 61 (2016) 315-360.
- [3] O. K. Chopra and A. S. Rao, A review of irradiation effects on LWR core internal materials Neutron embrittlement, J. Nucl. Mat. 412 (2011) 195-208.
- [4] T.S. Byun, B.E. Garrison, M.R. McAlister, X. Chen, M.N. Gussev, T.G. Lach, A.Le Coq,K.Linton, C.B. Joslin, J.K. Carver, F.A. List, R.R. Dehoff, K.A. Terrani, Mechanical behavior of additively manufactured and wrought 316L stainless steels before and after neutron irradiation, J. Nucl. Mat. 548 (2021) 152849.

- [5] J. Simpson, J. Haley, C. Cramer, O. Shafer, A. Eilliott, W. Peter, L. Love, R. Dehoff, Considerations for Application of Aadditive Manufacturing to Nuclear ReactorCore Components, Oak Ridge National Laboratory, 2019 ORNL/TM-2019-1190.
- [6] T. Ronneberg, C.M. Davies, P.A. Hooper, Revealing relationships between porosity, microstructure and mechanical properties of laser powder bed fusion 316LStainless steel through heat treatment, Mater. Des. 189 (2020) 108481.
- [7] U.S. Bertoli , B.E. MacDonald , J.M. Schoenung , Stability of cellular microstructurein laser powder bed fusion of 316L stainless steel, Mater. Sci. Eng. A 739 (2019) 109117 .
- [8] T.S. Byun, M.N. Gussev, T.G. Lach, M.R. McAlister, J.J. Simpson, B.E. Garrison, Y.Yamamoto, C.B. Joslin, J.K. Carver, F.A. List, R.R. Dehoff, K.A. Terrani, M. Li, X.Zhang, Mechanical Properties and Deformation Behavior of Additively Manufactured 316L Stainless Steel FY 2020, Oak Ridge National Laboratory, 2020ORNL/TM-2020/1574.
- [9] D. Kong , X. Ni , C. Dong , L. Zhang , C. Man , X. Cheng , X. Li , Anisotropy in themicrostructure and mechanical property for the bulk and porous 316L stainlesssteel fabricated via selective laser melting, Mater. Lett. 235 (2019) 15.
- [10] T. Kurzynowski, K. Gruber, W. Stopyra, B. Ku znicka, E. Chlebus, Correlation be-tween process parameters, microstructure and properties of 316 L stainlesssteel processed by selective laser melting, Mater. Sci. Eng. A 718 (2018) 6473.
- [11] G.T. Gray III, V. Livescu, P. A. Rigg, C.P. Trujillo, C.M. Cady, S.R. Chen, J.S. Carpenter, T.J. Lienert, S.J. Fensin, Structure/property (constitutive and spallation response) of additively manufactured 316L stainless steel. Acta Mater. 138 (2017) 140149.
- [12] l. Liu L, Q. Ding, Y. Zhong, et al., Dislocation network in additive manufactured steel breaks strengthductility trade-off. Mater Today. 21 (2018) 354361. inclusions in 316L stainless steel manufactured by laser powder bed fusion and its influence on impact toughness
- [13] E. Garlea, H. Choo, C.C. Sluss, M.R. Koehler, R.L. Bridges, X. Xiao, Y. Ren, B.H. Jared, Variation of elastic mechanical properties with texture, porosity, and defect characteristics in laser powder bed fusion 316L stainless steel, Mater. Sci. Eng. A 763 (2019) 138032.
- [14] T. Pinomaa, M. Lindroos, M. Walbrhl, N. Provatas, A. Laukkanen, The significance of spatial length scales and solute segregation in strengthening rapidsolidification microstructures of 316L stainless steel, Acta Mater. 184 (2020) 116.

- [15] M. Li, X. Zhang, W.Y. Chen, F. Heidet, T.S. Byun, K.A. Terrani, Creep behavior of 316L stainless steel manufactured by laser powder bed fusion, J. Nucl. Mater. 548 (2021) 152847.
- [16] P. Deng, M. Song, J. Yang, Q. Pan, S. McAllister, L. Li, B. C. Prorok, X. Lou, On the thermal coarsening and transformation of nanoscale oxide, Materials Science and Engineering: A 835 (2022) 142690.
- [17] E. de Sonis, S. Depinoy, Pierre-Francois Giroux, H. Maskrot, P. Wident, O. Hercher, F. Villaret, A.-F. Gourgues-Lorenzon, Microstructure Toughness relationships in 316L stainless steel produced by laser powder bed fusion, Materials Science and Engineering: A 877 (2023) 145179.
- [18] Z. Shang, C. Fan, S. Xue, Jie Ding, Jin Li, T. Voisin, Y. M. Wang, H. Wang and X. Zhang, Response of solidification cellular structures in additively manufactured 316 stainless steel to heavy ion irradiation: an in situ study, Materials Research Letters, 7 (2019) 290-297.
- [19] T. Voisin, J.-B. Forien, A. Perron, S. Aubry, N. Bertin, A. Samanta, A. Baker, and Y. M. Wang, New insights on cellular structures strengthening mechanisms and thermal stability of an austenitic stainless steel fabricated by laser powder-bed-fusion, Acta Mat. 203 (2013) 116476.
- [20] O.O. Salman, C. Gammer, A. K. Chaubey, J. Eckert, S. Scudino, Effect of heat treatment on microstructure and mechanical properties of 316L steel synthesized by selective laser melting, Mat. Sci. Eng. A, 748 (2019) 205-212.
- [21] X. Lou, P. L. Andresen, R. B. Rebak, Oxide inclusions in laser additive manufactured stainless steel and their effects on impact toughness and stress corrosion cracking behavior, J. Nucl. Mat., 499 (2018) 182-190.
- [22] X. Wang, O. Sanchez-Mata, S. Ece Atabay, J. A. Muñiz-Lerma, M. A. Shandiz, M. Brochu, Crystallographic orientation dependence of Charpy impact behaviours in stainless steel 316L fabricated by laser powder bed fusion, Additive Manufacturing 46 (2021) 102104.
- [23] NEI, Roadmap for Regulatory Acceptance of Advanced Manufacturing Methods in the Nuclear Energy Industry, 2019.
- [24] G. Meric de Bellefon, K.M. Bertsch, M.R. Chancey, Y.Q. Wang, D.J. Thoma, Influence of solidification structures on radiation-induced swelling in an additively-manufactured austenitic stainless steel, J. Nucl. Mat. 523 (2019) 291-298.
- [25] J. Lin, F. Chen, X. Tang, J. Liu, S. Shen, G. Ge, Radiation-induced swelling and hardening of 316L stainless steel fabricated by selected laser melting, Vacuum 174 (2020) 109183.

- [26] M. Loyer-Prost, A-H Puichaud, C. Flament, E. Rouesne, J-L Béchade aImpact of intragranular misorientation on void swelling and inter-granular cavities after ion irradiation in standard and additive manufacturing 316L austenitic steels, J. Nucl. Mat. 573 (2023) 154102.
- [27] M. Song , M. Wang , X. Lou , R.B. Rebak , G.S. Was , Radiation damage and irradi- ation-assisted stress corrosion cracking of additively manufactured 316L stain- less steels, J. Nucl. Mater. 513 (2019) 3344 .
- [28] D. Bardel *et.al*. Additive manufacturing for fuel components: An overview of key achievements at Framatome, Top Fuel 2021 conference, Santander, Spain.
- [29] P.D. Freyer et.al. Hot cell tensile testing of neutron irradiated additively Manufactured type 316L Stainless steel. Proceeding of the A_{th} international conference on Environmental Degradation of Materials in Nuclear Power Sytems - Water Reactors, The Minerals, Metals and Materials, 2018.
- [30] NUCOBAM: NUclear COmponents Based on Additive Manufacturing. EU-funded project grant 945313. https://nucobam.eu/, https://cordis.europa.eu/project/id/945313/fr
- [31] ISO/ASTM 52911 :2019. Additive manufacturing Design. Par 1 : Laser-based powder bed
- [32] ISO 14556, Steel Charpy V-notch pendulum impact test Instrumented test method
- [33] ASTM E21, Standard Test Methods for Elevated Temperature Tension Tests of Metallic Materials
- [34] Materials reliability program: Development of a material constitutive model for irradiated austenitic stainless steels (MRP135 Revision2), EPRI 2019 technical report.